Supplementary Information (SI) for Materials Horizons.

Supplementary Information

Heterogeneous nanocomposite architecture with contrasting thermal conductivity and hydrophilicity for synergistic solar-thermal storage and evaporation

Kit-Ying Chan[1,2], Xiuli Dong[1], Yunfei Yang[1], Xiaomeng Zhao[1], Duo Li[1], Mengyang Xu[5], Xuemin Yin[1], Zhenyu Wang[4], Xi Shen[1,2,3]*

[1] Department of Aeronautical and Aviation Engineering, The Hong Kong Polytechnic University, Hong Kong SAR, China

[2] The Research Institute for Advanced Manufacturing, The Hong Kong Polytechnic University, Hong Kong SAR, China

[3] The Research Institute for Sports Science and Technology, The Hong Kong Polytechnic University, Hong Kong SAR, China

[4] School of Mechanical Engineering, Jiangnan University, Wuxi, China

[5] Department of Chemical and Biological Engineering, The Hong Kong University of Science and Technology, Hong Kong, China

*Corresponding author: xi.shen@polyu.edu.hk (X.S.)

Note S1. Fabrication of TSC for thermal storage

3D graphene structures were fabricated on Ni foam template by chemical vapor deposition (CVD).[1] In brief, the Ni microlattice template was cleaned and pre-treated before putting in the quartz tube of CVD furnace. The tube furnace was firstly heated to 900°C in 40 minutes and kept for 20 minutes with the supply of pure H_2 (100 sccm) and Ar (200 sccm) to remove dust on the Ni meshes. Then, the flow of C_2H_4 (10 sccm) was introduced for 20 minutes in addition to the presence of H_2 and Ar. Then, the flow of C_2H_4 was stopped and the furnace was cooled down rapidly to room temperature with the flow of Ar (200 sccm) to avoid any oxidation of graphene. Afterwards, the Ni template was removed by immersing the graphene/Ni meshes in the $FeCl_3$ solution at ambient condition for 48 hours. After the etching of the Ni template, a free-standing graphene foam with pore size of several hundred micrometers was obtained. Paraffin wax (PW) (Aladdin, melting temperature of 52 – 54°C) used as phase change material (PCM) was melted at 70°C and mixed with 5wt% carbon nanotubes (CNTs) for enhanced thermal conductivity and solar absorption. Then, the CNTs/PW mixture was infiltrated into the porous graphene structure using a vacuum oven at 70°C. Before cooling down to room temperature, the oven was kept in vacuum condition to avoid any void in the TSC. The center of solidified TSC was cut and integrated with the GHE as an ISTSE device.

Note S2. Fabrication of GHE and the integrated device

A polyvinyl alcohol (PVA) solution with a concentration of 5 wt% was obtained by dissolving PVA powders with a molecular weight ranging 89,000 – 98,000 (Sigma Aldrich) in deionized (DI) water at 90°C with stirring for 2 hours. The PVA solution was then mixed with a GO solution (Ashine, concentration of 20 mg ml^{-1}) at a loading of 10 wt% under vigorous stirring for 30 min, followed by cooling to room temperature before performing fan-shaped freeze-casting technique, as shown in Fig. 2a. The ice crystals grew in a radiating pattern from the center cold source to peripherals. The frozen sample was placed in a freezer at -40°C overnight to allow the completion of physicochemical crosslinking, followed by thawing at ambient condition to obtain GHE.[2, 3] Afterward, the GHE was placed at the center of TSC to form an integrated device, as shown in Fig. 1a and b. The gradient structures can be controlled through different approaches such as tailoring the solid content in colloidal solution and freezing temperature for freeze-casting, which were reported in our previous study. [4, 5] The solid content in the colloidal solution plays a crucial role in determining the final pore size and density. Higher solid content resulted in smaller pores and thicker cell walls, while lower solid content led to larger pores and thinner cell walls, as shown in Fig. S3. The temperature of the cold source used in freeze-casting is another critical factor. By adjusting the temperature gradient during the freezing process, the rate of ice crystal growth can be controlled, which in turn affects the pore structure. For instance, a higher freezing temperature of – 40 °C was used to fabricate gradient materials instead of using liquid nitrogen (– 196 °C). It can be seen from Fig. S4 that the pore sizes of gradient material produced using a higher freezing temperature were much larger than those produced using a lower freezing temperature.

Note S3. Characterization

The microstructures of GO/PVA hydrogels and TSC were characterized by a scanning electron microscopy (SEM, Hitachi TM3030). The water content of GHE was calculated by $Water\ content = \frac{m_{hydrogel} - m_{aerogel}}{m_{hydrogel}} \times 100\%$, where $m_{hydrogel}$ is the mass of hydrogel after freeze-thawing and $m_{aerogel}$ is the mass of aerogel after freeze-drying of the same hydrogel. The functional groups on PVA, GO and GO/PVA hydrogels were studied using the FTIR (Bruker Vertex 70 Hyperion 1000). The solar absorption was calculated by $\alpha = 1 - R - T$, where R is the reflectance and T is the transmittance of samples. Both R and T were determined using an ultraviolet (UV)-visible-near infrared (NIR) spectrometer (Perkin Elmer Lambda 950) in a wavelength range of 0.25 –2.5 µm. The solar weighted absorption was calculated according to the specification, ASTM G173-03. The thermal conductivity (*k*) of samples was measured using a hot disk thermal constant analyzer (Hot Disk TPS 2500 S) with isotropic measurements for TSC samples and anisotropic modes for hydrogel evaporators. The heat capacity of TSC was obtained using differential scanning calorimeter (DSC, Mettler Toledo).

Note S4. Water generation setup

The water generation tests were carried out using a customized setup. The setup included a solar irradiation simulator (Xenon lamp, PLS-SXE300) with a solar filter and diffuser to ensure the solar spectrum range and uniform light intensity, and an analytical balance (FA 2004) with an accuracy of 0.1mg. The light intensity was measured using a solar meter (TES-1333R Solar Power Meter). The test setup was enclosed in an environmental chamber with interior temperature of ~25°C and humidity of ~45% under a breezeless condition and covered by a blackout curtain. The analytical balance was connected to a computer to record the time-dependent mass change of water due to steam generation. The surface temperatures of GHE and TSC during the water generation tests were monitored using the thermocouples (CENTER-309 Portable Digital Thermometer).

Note S5. Numerical simulation

COMSOL Multiphsics software (6.3 Version) was used to simulate the heat transfer between the TSC and hydrogel evaporators (VHE and GHE) in the integrated devices. The simulated devices with the same structure scale as GHE-TSC and VHE-TSC were constructed respectively.

5.1 Simulation of radiation-induced heat on the TSC-GHE and TSC-VHE using COMSOL.

To simulate the thermal change caused by the external radiation flux on the material surface, surface-to-surface radiation heat transfer was added to construct the surface heat flux. The formula utilised in the 2D model is:

$$-n \cdot q = q_{r,\mathrm{net}} \qquad \text{Eq. (1)}$$

where n is the unit normal vector indicating the direction of heat flow, q is the heat flow density vector indicating the heat flow per unit area, and $q_{r,net}$ is the net radiant heat flow indicating the energy transfer from the radiant source.

5.2 Simulation of heat transfer from solid, fluid and wet surfaces for TSC-GHE and TSC-VHE using COMSOL.

Considering the solid-fluid heat transfer inside the material and the latent heat of evaporation due to the evaporation effect through the wet surface, the heat transfer processes and temperature changes inside and on the surface of the material were simulated using heat and moisture transfer model. The equations utilised in the 2D model are as follows:

$$\rho C_p \frac{\partial T_2}{\partial t} + \rho C_p u \cdot \nabla T_2 + \nabla \cdot q = Q + Q_p + Q_{vd} \qquad \text{Eq. (2)}$$

$$q = -k \nabla T_2 \qquad \text{Eq. (3)}$$

where ρ is the density; C_p is the constant pressure specific heat, which indicates the amount of heat required to raise the temperature of a substance per unit mass at constant pressure; u is the velocity vector of the fluid; ∇T_2 is the temperature gradient; q is the heat flow density. In addition, Q is the external heat source term, which represents all heat sources in the system except viscous dissipation;

Q_p is the work done by the pressure change, which is usually associated with heating during adiabatic compression, as well as thermoacoustic effects; Q_{vd} denotes viscous dissipation in the fluid and represents the heat produced by the fluid due to viscous effects, and k is the thermal conductivity.

The phase transition process of TSC was incorporated in the heat transfer simulation to calculate the heat storage and exchange carried out by PCM. Since the maximum surface temperature of TSC under one-sun was around ~40°C, only solid-solid transition occurred. As such, the single-phase transition performed by PCM was used in the 2D model by the following equations:

$$\rho = \rho_{\text{solid}} \qquad \text{Eq. (4)}$$

$$c_p = \theta_1 C_{p1} + \theta_2 C_{p2} + L_{1\to 2}\frac{\partial \alpha_m}{\partial T} \qquad \text{Eq. (5)}$$

$$\alpha_m = \frac{1}{2}\theta_2 - \theta_1 + \theta_2 \qquad \text{Eq. (6)}$$

$$k = \theta_1 k_1 + \theta_2 k_2 \qquad \text{Eq. (7)}$$

$$\theta_1 + \theta_2 = 1 \qquad \text{Eq. (8)}$$

where $L_{1\to 2}$ denotes the latent heat from phase 1 to phase 2; α_m represents the phase transition correlation coefficient, which is determined by the mass fractions θ_1 and θ_2 of the two phases during the phase transition.

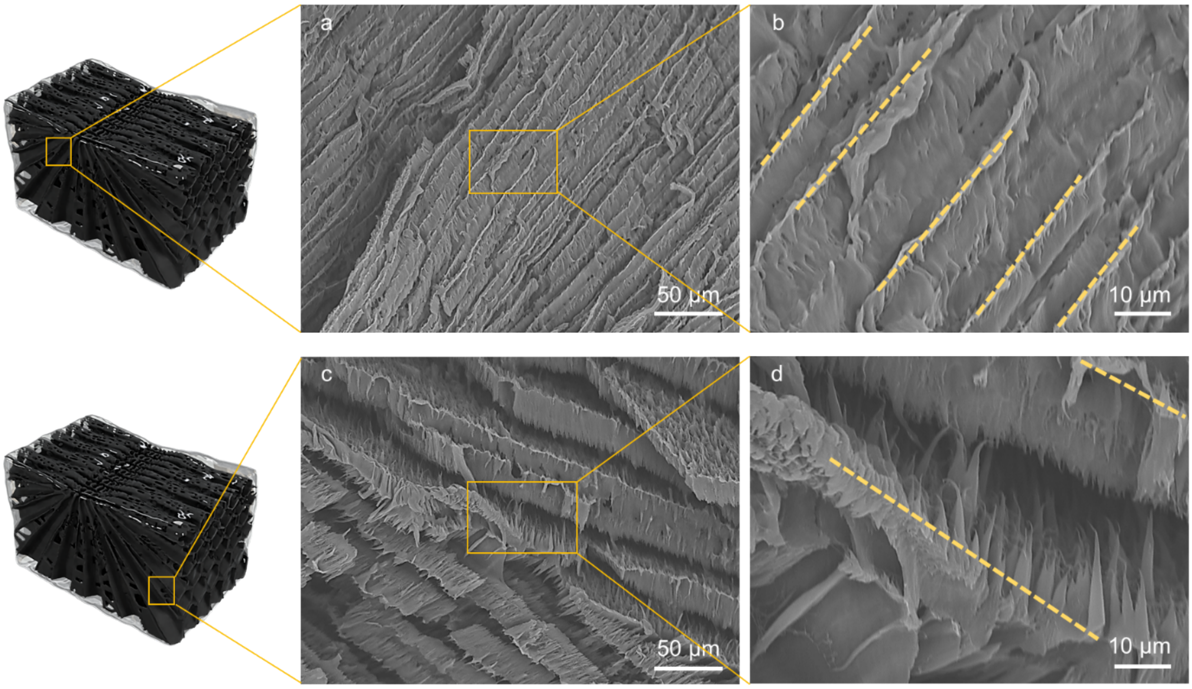

Fig. S1. SEM images showing the pore channels of GHE in radiating pattern with (a,b) smaller pore size near the evaporation surface (water outlet) and (c,d) larger pore size away from the evaporation surface (water inlet).

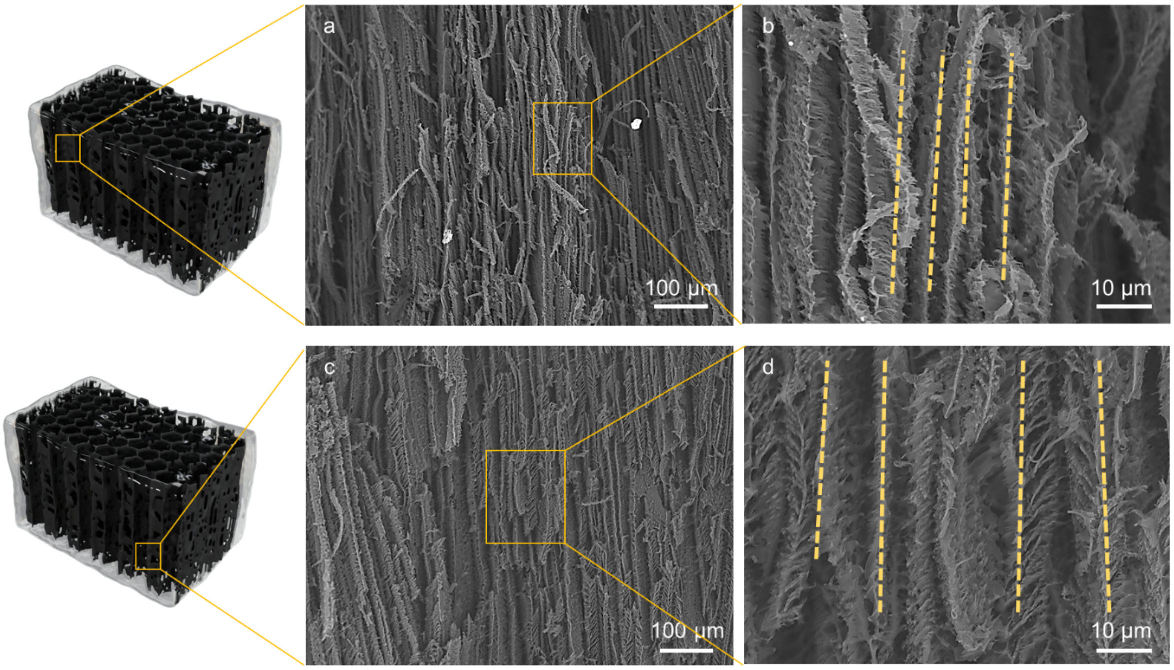

Fig. S2. SEM images showing the pore channels of VHE in vertical direction with (a,b) smaller pore size near the evaporation surface (water outlet) and (c,d) larger pore size away from the evaporation surface (water inlet).

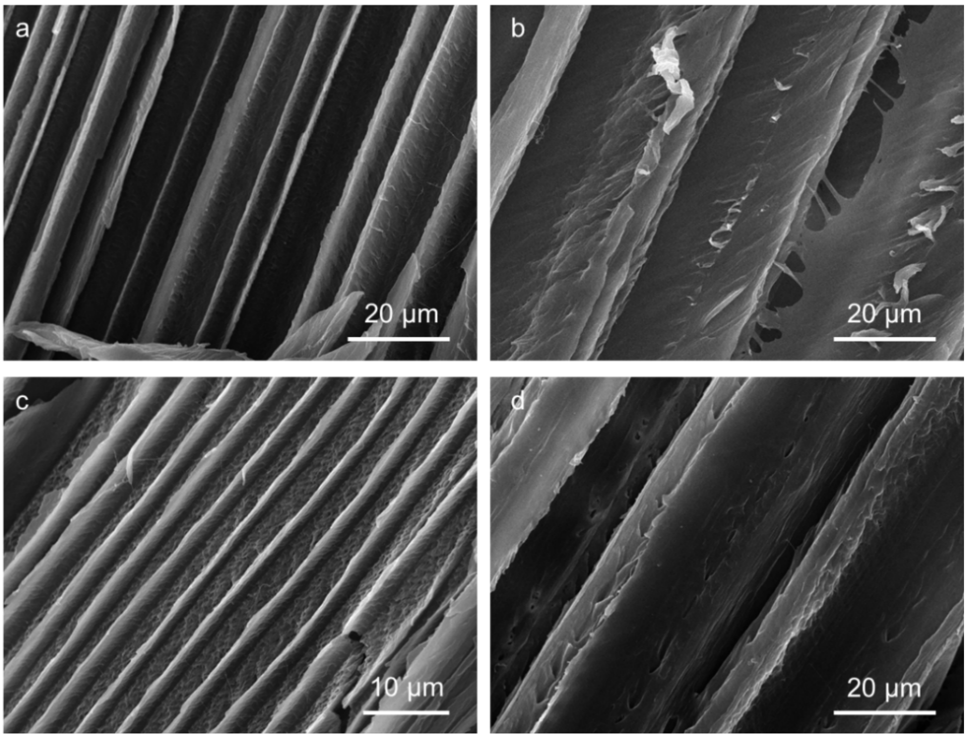

Fig. S3. SEM images showing the pore channels of PVA aerogels in radiating pattern with (a,b) lower PVA content and (c,d) higher PVA content.

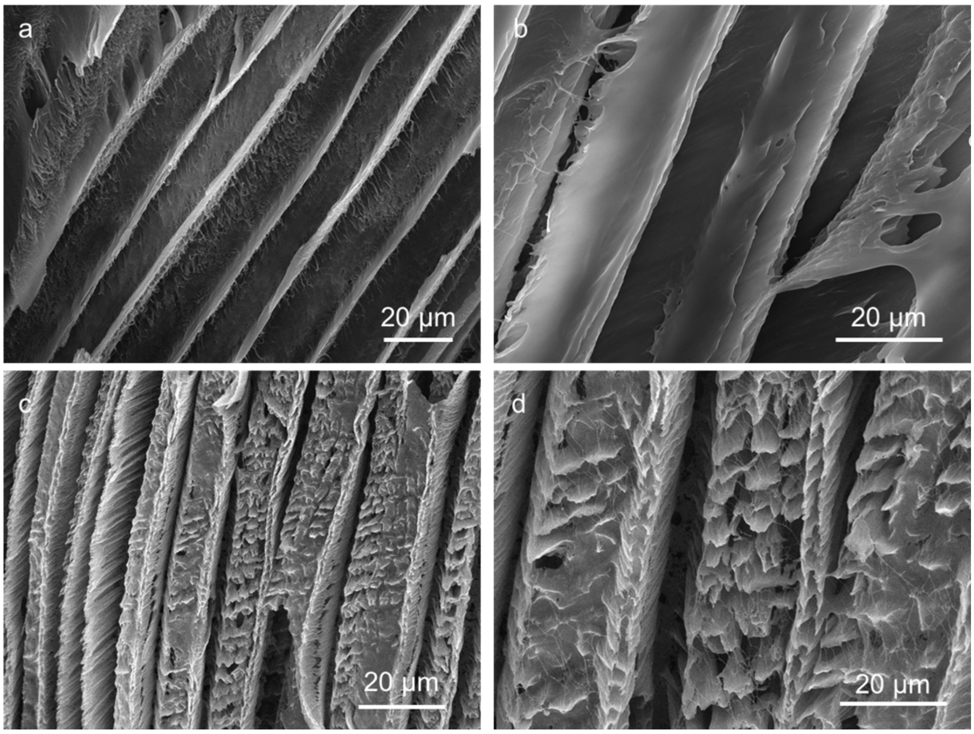

Fig. S4. SEM images showing the pore channels of PVA aerogels in radiating pattern with (a,b) a lower freezing temperature and (c,d) a higher freezing temperature.

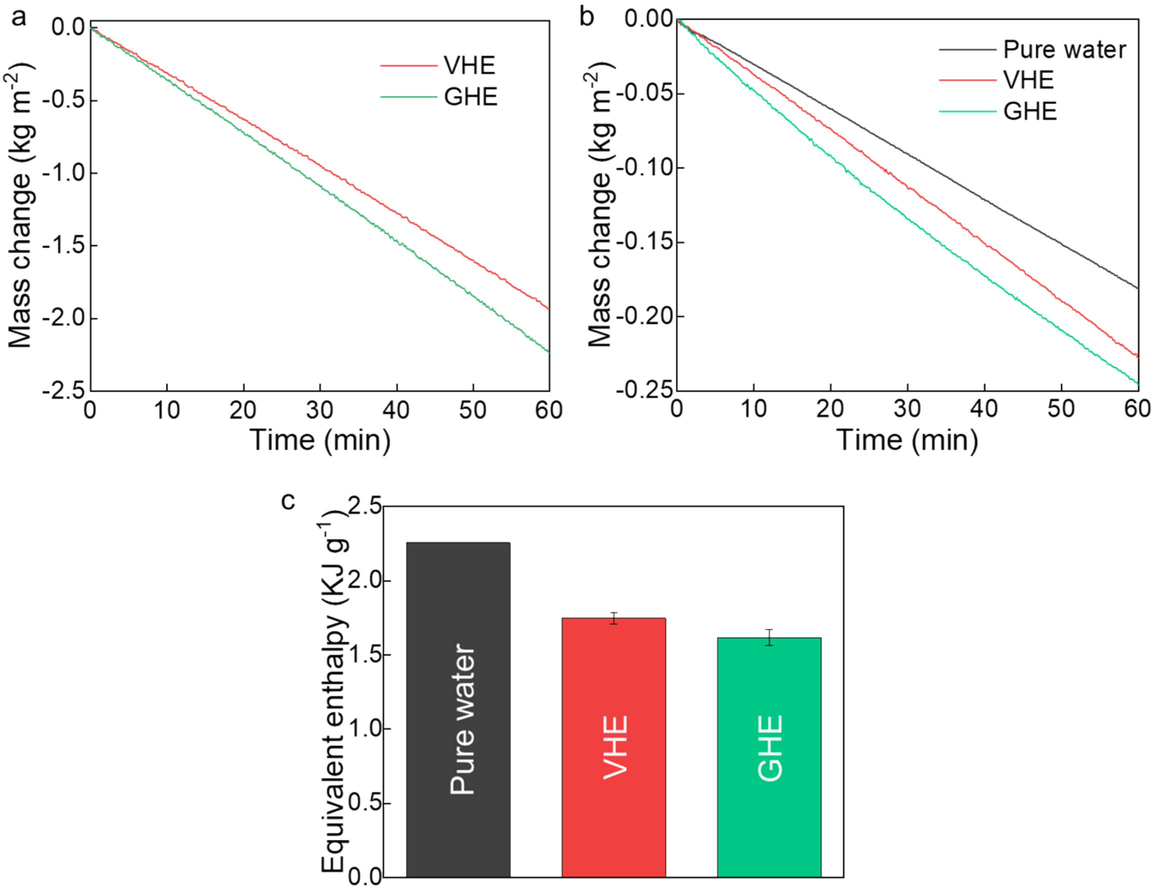

Fig. S5. Time-dependent mass changes of VHE and GHE (a) under solar intensity of 1 kW m^{-2} and (b) in dark condition. (c) The corresponding equivalent enthalpy of vaporization of VHE and GHE.

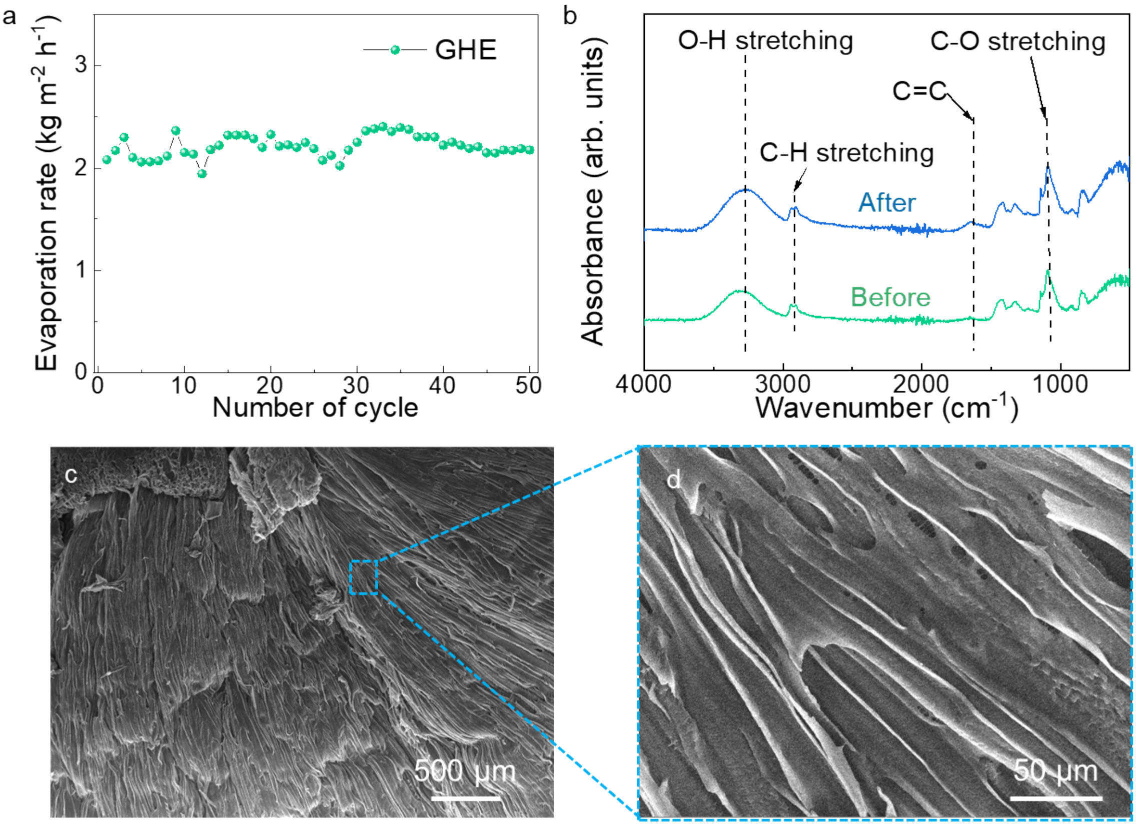

Fig. S6. (a) Long-term evaporation rates of GHE under one-sun illumination. (b) FTIR spectra of freeze-dried GHE before and after 50 cycles of evaporation tests. (c,d) SEM images of GHE after the test at various magnifications.

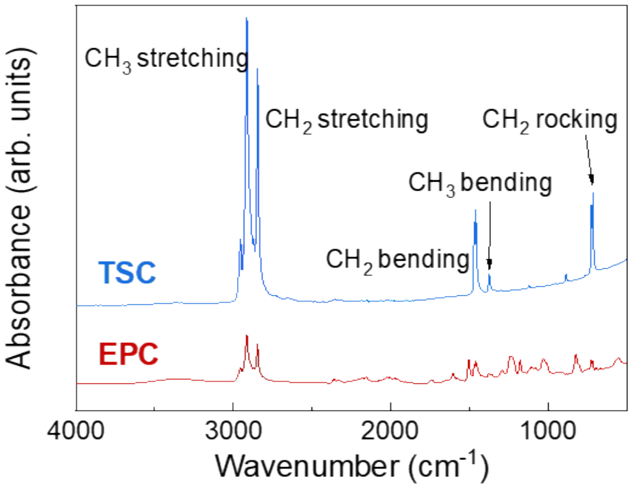

Fig. S7. FTIR spectra showing few oxygen-containing functional groups of TSC and EPC.

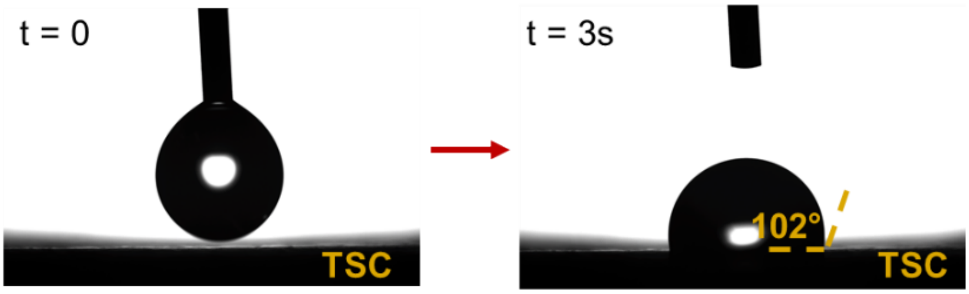

Fig. S8. Contact angle of TSC at different times.

Fig. S9. Digital image showing the sinking of GHE alone.

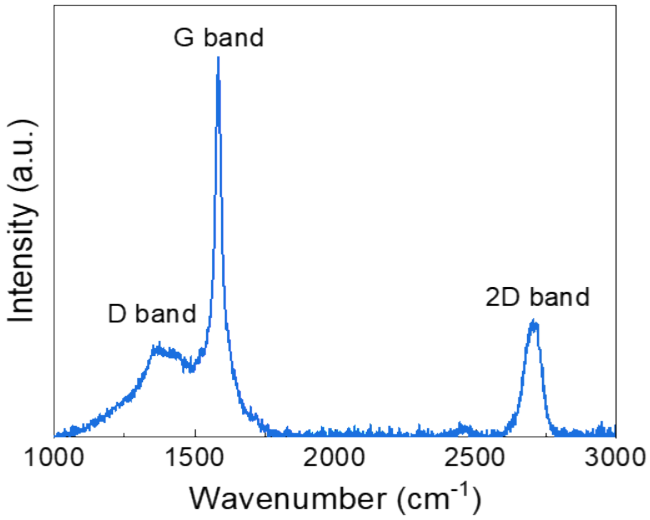

Fig. S10. Raman spectroscopy of CVD-grown graphene.

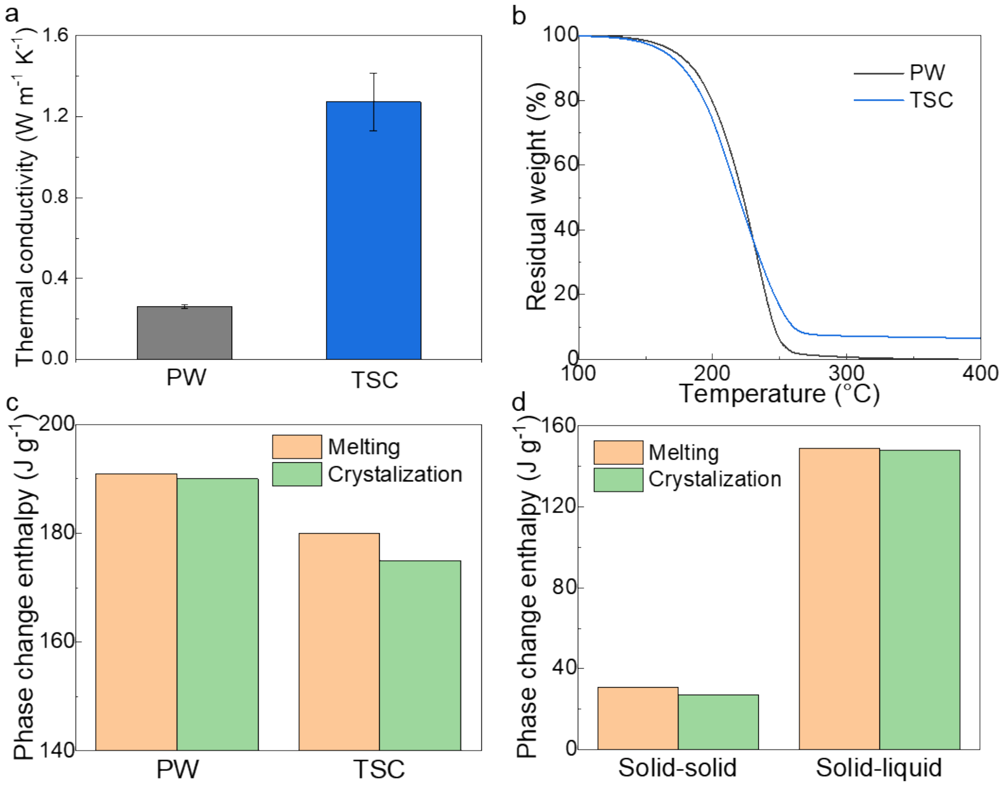

Fig. S11. (a) Thermal conductivity (*k*), (b) TGA and (c) phase change enthalpy of melting and crystallization of pristine PW and TSC. (d) Solid-solid and solid-liquid phase change enthalpy of TSC.

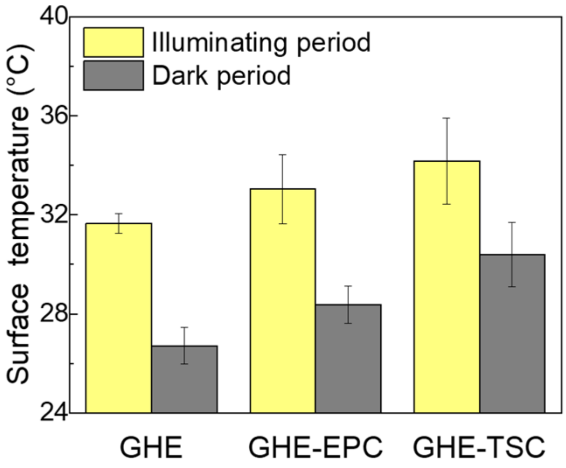

Fig. S12. Average evaporation surface temperatures of three evaporators during three illumination-dark cycles under one sun.

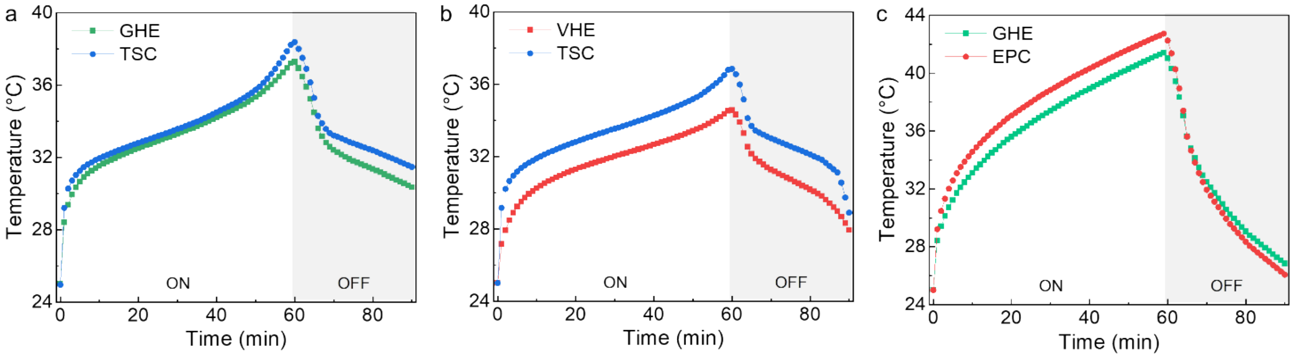

Fig. S13. Temperature profiles of hydrogel evaporator and EPC/TSC in the integrated devices of (a) GHE-TSC, (b) VHE-TSC and (c) GHE-EPC.

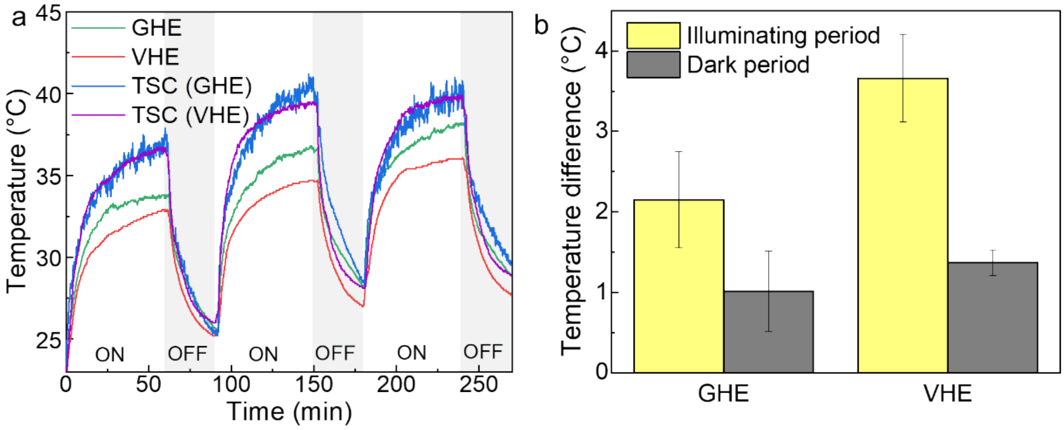

Fig. S14. (a) Surface temperatures in the integrated devices using GHE-TSC and VHE-TSC. (b) Difference in average surface temperatures between TSC and GHE, and TSC and VHE.

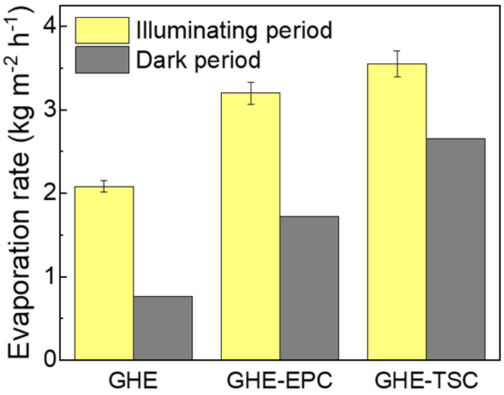

Fig. S15. Average evaporation rates of three evaporators during three illumination-dark cycles under one sun.

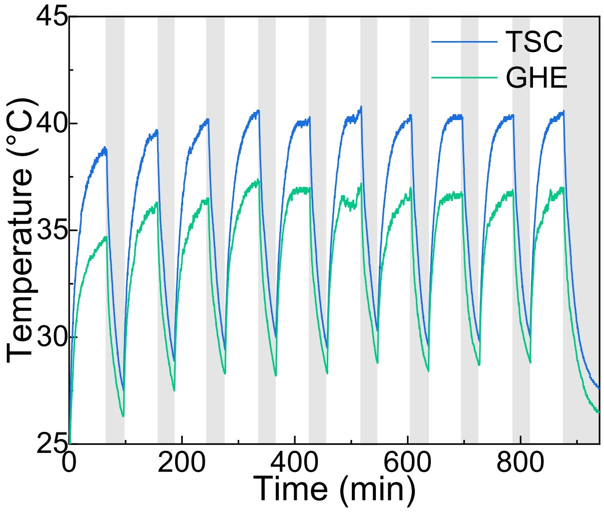

Fig. S16. Temperature profiles of TSC and GHE during ten illumination-dark cycles under 1 sun.

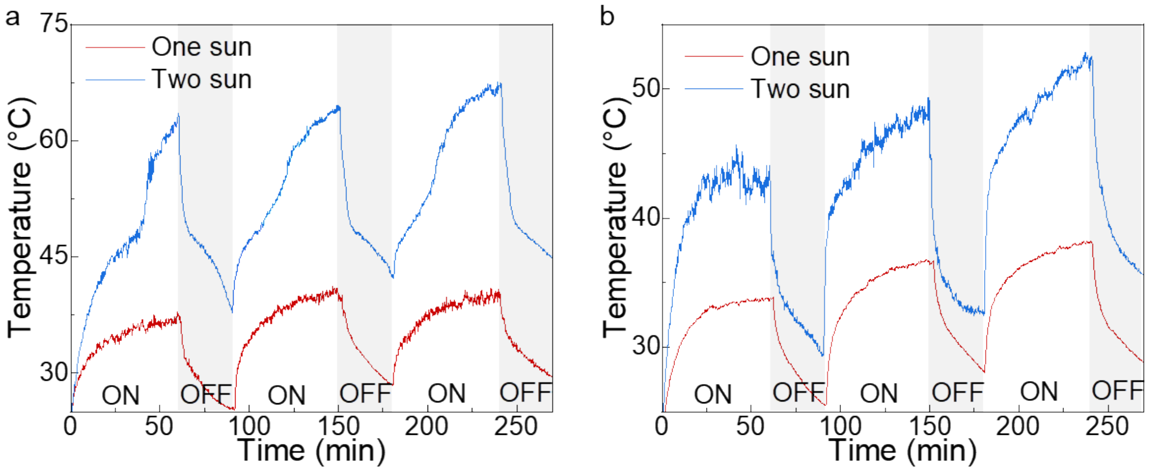

Fig. S17. Temperature profiles of (a) TSC and (b) GHE equipped with TSC during three illumination-dark cycles under 1 sun and 2 sun.

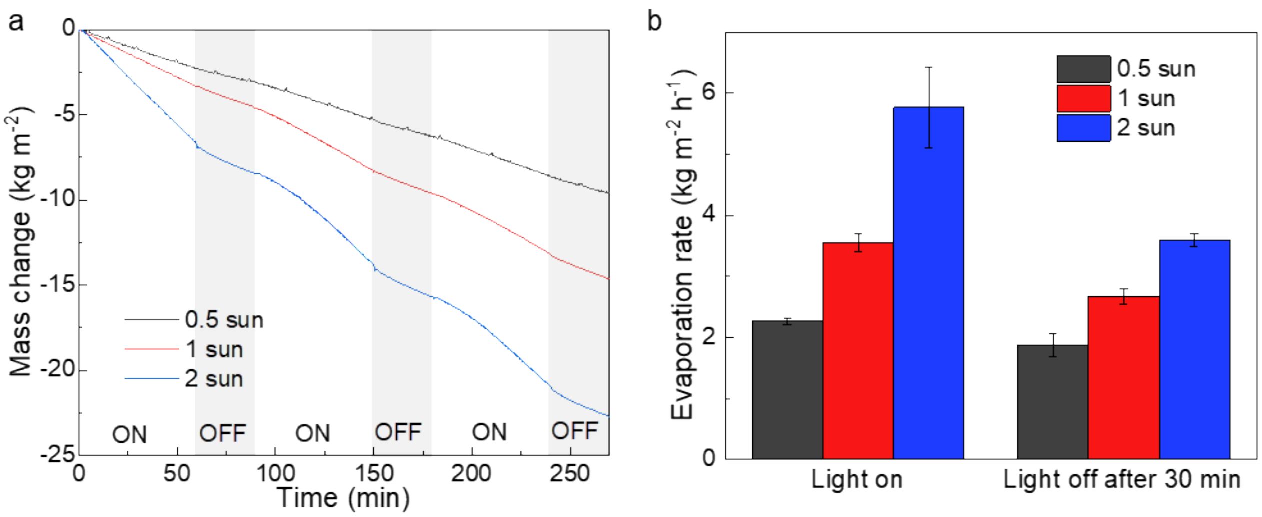

Fig. S18. (a) Time-dependent mass changes and (b) average evaporation rates of integrated device during three illumination-dark cycles under 0.5 sun, 1 sun and 2 sun.

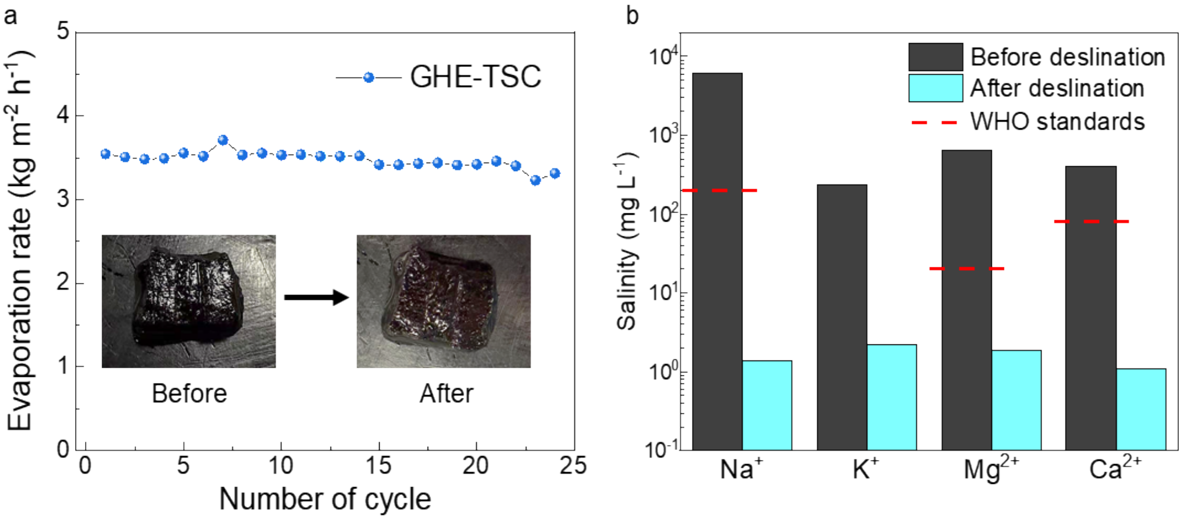

Fig. S19. (a) Evaporation rates of ISTSE device in 24-hour continuous seawater evaporation under one-sun illumination. The inset shows that no salt crystals are formed on the evaporation after the test. (b) Comparison of the concentration of metal ions in seawater and condensed freshwater.

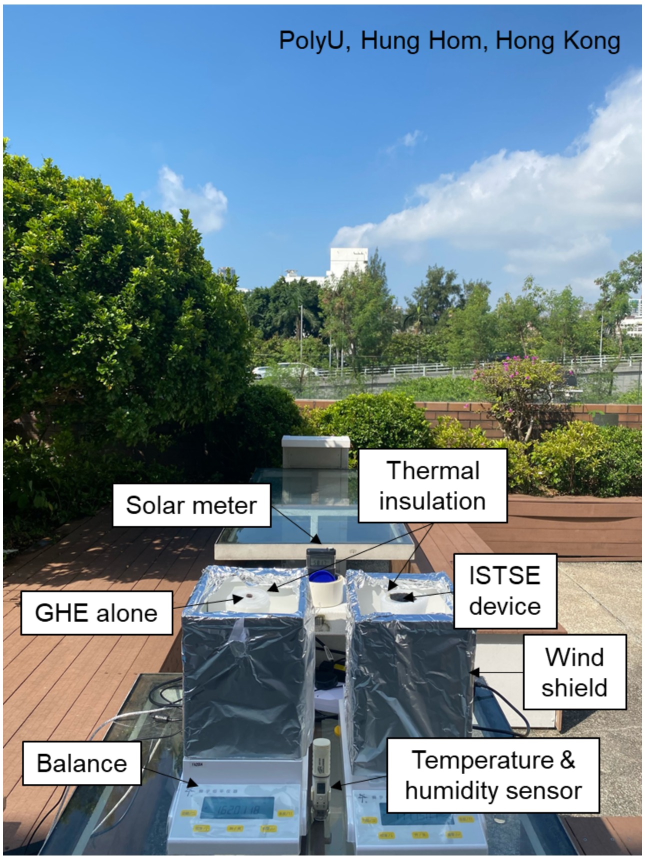

Fig. S20. Image of the experimental setup comprising of two test devices (i.e., ISTSE device and GHE alone), thermal insulation, two weight balances connected to computers, a solar meter and a temperature and humidity sensor.

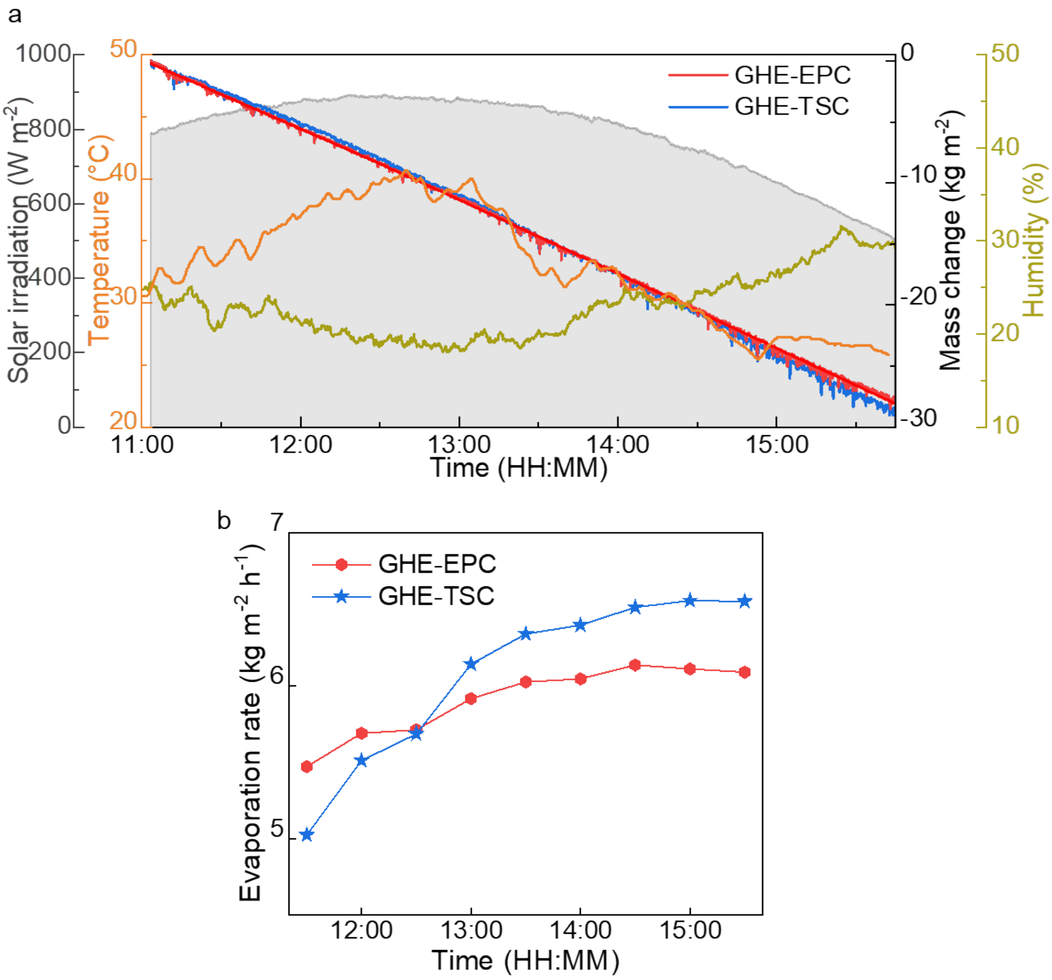

Fig. S21 (a) Mass changes of water using GHE-EPC and GHE-TSC devices, solar irradiation, ambient temperature, and humidity during the outdoor test on 19th March 2025. (b) Evaporation rates of GHE-EPC and GHE-TSC devices.

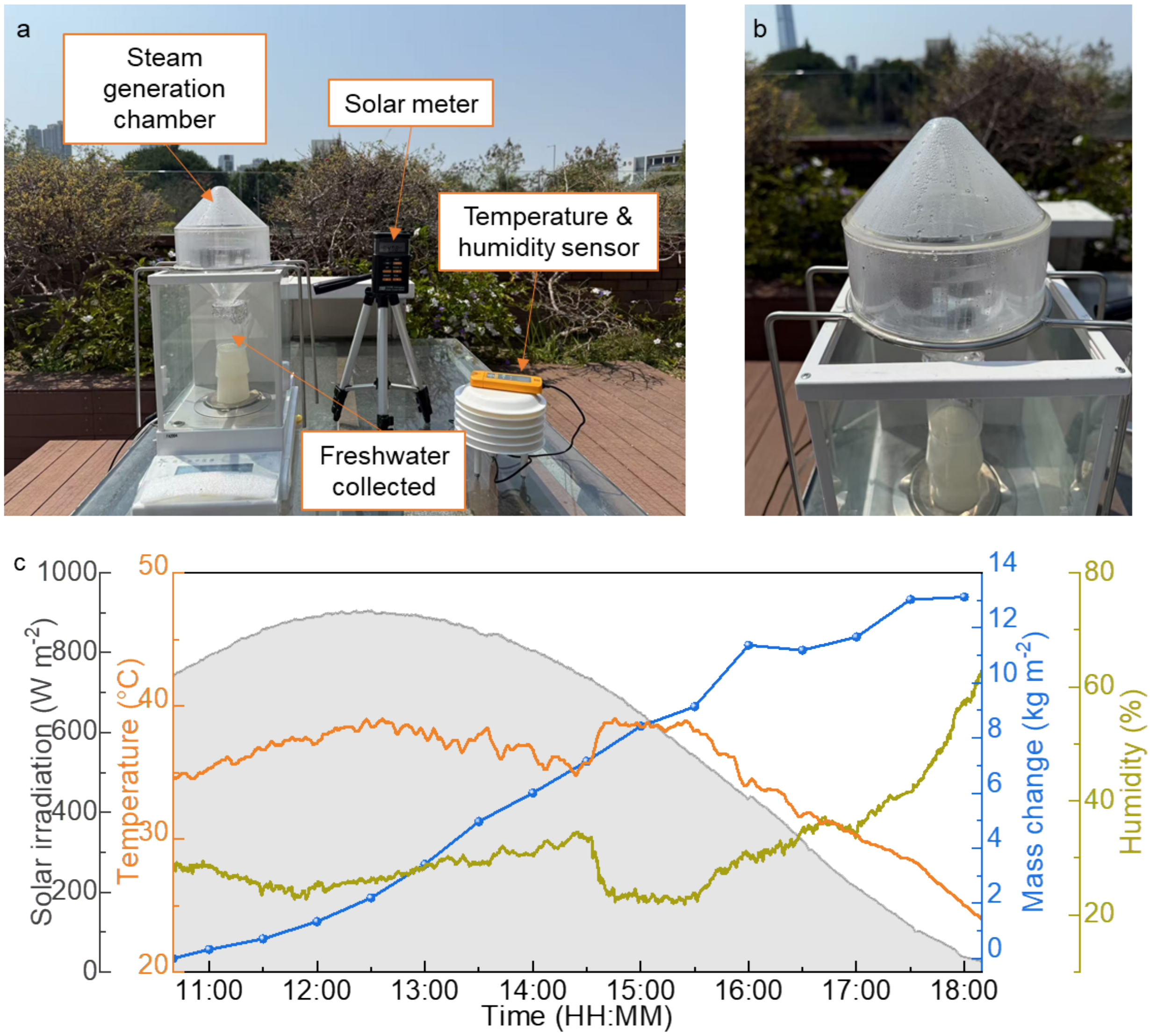

Fig. S22 (a) Set-up for freshwater collection. (b) Digital image showing that the condensed water droplets on the inner surface after half an hour of direct sunlight, demonstrating an efficient water collection. (c) Mass change of water collection using ISTSE device, solar irradiation, ambient temperature, and humidity during the test on 25th March 2025.

Reference

1. X. Liu, D. Liu, J. H. Lee, Q. Zheng, X. Du, X. Zhang, H. Xu, Z. Wang, Y. Wu, X. Shen, J. Cui, Y. W. Mai and J. K. Kim, *ACS Appl. Mater. Interfaces*, 2019, **11**, 2282-2294.
2. Q. Yan, R. Ding, H. Zheng, P. Li, Z. Liu, Z. Chen, J. Xiong, F. Xue, X. Zhao, Q. Peng and X. He, *Adv. Funct. Mater.*, 2023, **33**, 2301982.
3. L. Zhang, J. Zhao, J. Zhu, C. He and H. Wang, *Soft Matter*, 2012, **8**, 10439-10447.

4. K.-Y. Chan, X. Shen, J. Yang, K.-T. Lin, H. Venkatesan, E. Kim, H. Zhang, J.-H. Lee, J. Yu and J. Yang, *Nat. Commun.*, 2022, **13**, 5553.
5. E. Kim, K.-Y. Chan, J. Yang, H. Venkatesan, M. H. Adegun, H. Zhang, J.-H. Lee, X. Shen and J.-K. Kim, *J. Mater. Chem. A*, 2023, **11**, 7105-7114.